



Near-Earth High-Speed and Slow Solar Winds: A Statistical Study on Their Characteristics and Geomagnetic Impacts

Rajkumar Hajra^{1,2}

Received: 9 November 2022 / Accepted: 7 March 2023
© The Author(s), under exclusive licence to Springer Nature B.V. 2023

Abstract

Near-Earth solar winds are separated into two groups: slow solar wind (SSW) with plasma speed $[V_{sw}] < 500 \text{ km s}^{-1}$ and high-speed solar wind (HSW) with $V_{sw} > 700 \text{ km s}^{-1}$. A comparative study is performed on the plasma and interplanetary magnetic field (IMF) properties of the near-Earth SSW and HSW, using solar wind measurements propagated to Earth's bow shock nose from 1963 through 2022. On average, HSW is characterized by higher alpha-to-proton density ratio $[N_a/N_p]$ (67%), ram pressure $[P_{sw}]$ (95%), proton temperature $[T_p]$ (370%), reconnection electric field $[V B_s]$ (141%), Alfvén speed $[V_A]$ (76%), magnetosonic speed $[V_{ms}]$ (65%), and lower proton density $[N_p]$ (52%) and plasma- β (54%) than SSW. In $V B_s$, $V = V_{sw}$, B_s is the southward component of IMF. $V_A = B_0 / \sqrt{\mu_0 \rho}$, $V_{ms} = \sqrt{V_A^2 + V_s^2}$, where B_0 is the IMF magnitude, μ_0 is the free space permeability, ρ is the solar wind mass density, and V_s is the sound speed. β is defined as the plasma pressure to the magnetic-pressure ratio. The geomagnetic activity is found to be enhanced during HSW, as reflected in higher average auroral electrojet index [AE] (213%) and stronger geomagnetic Dst index (367%) compared to those during SSW. The SSW characteristic parameters N_a/N_p , T_p , B_0 , V_A , and V_{ms} exhibit medium to strong correlations (correlation coefficients $r = 0.51$ to 0.87) with the $F_{10.7}$ solar flux, while β and Mach numbers exhibit strong anti-correlations ($r = -0.82$ to -0.90) with $F_{10.7}$. The associations are weaker or insignificant for HSW.

Keywords Solar wind · Solar cycle · Coronal holes · Coronal mass ejections, interplanetary · Magnetic fields, interplanetary · Magnetosphere, geomagnetic disturbances

1. Introduction

Solar winds have been broadly classified into two groups based on the plasma speed $[V_{sw}]$. They are: high-speed solar wind (HSW) with a peak V_{sw} in the range of $\approx 750\text{--}850 \text{ km s}^{-1}$

✉ R. Hajra
rajkumarhajra@yahoo.co.in; rhajra@ustc.edu.cn

¹ Indian Institute of Technology Indore, Indore 453552, India

² Present address: CAS Key Laboratory of Geospace Environment, School of Earth and Space Sciences, University of Science and Technology of China, Hefei, China

(Neugebauer and Snyder, 1966; Phillips et al., 1995; Tsurutani et al., 2006; Vršnak, Temmer, and Veronig, 2007; Verbanac et al., 2011a,b; Verbanac, Bandić, and Krauss, 2022, and references therein), and slow solar wind (SSW) with V_{sw} in the range of $\approx 350\text{--}450\text{ km s}^{-1}$ (Belcher and Davis, 1971; Abbo et al., 2016; Sanchez-Diaz et al., 2016; D'Amicis et al., 2021; Tsurutani and Hajra, 2022, and references therein). While HSW is known to originate from coronal holes (Krieger, Timothy, and Roelof, 1973), SSW possibly originates from helmet streamers of the Sun (Gosling et al., 1981; Suess et al., 2009; Abbo et al., 2016). Coronal hole emanated HSW is characterized by high-amplitude Alfvén waves (Belcher and Davis, 1971; Tsurutani et al., 2006), while SSW is mainly characterized by non-Alfvénic structures or low-amplitude Alfvén waves.

Earth is increasingly encountered by HSW during the solar cycle declining and minimum phases, when coronal holes dominate the solar equatorial region (Burlaga et al., 1978; Sheeley, Harvey, and Feldman, 1976; Sheeley and Harvey, 1981; Richardson, Cliver, and Cane, 2000; Tsurutani et al., 2006; Vršnak, Temmer, and Veronig, 2007; Verbanac et al., 2011a). Interaction of HSW with background (slow) wind results in a corotating interaction region (CIR) characterized by compressed (enhanced) plasma density and magnetic field (Davis, 1966; Davis et al., 1966; Belcher and Davis, 1971; Burlaga, 1974; Smith and Wolfe, 1976; Gosling et al., 1978; Pizzo, 1985; Vršnak et al., 2017; Hajra and Sunny, 2022; Sunny et al., 2023, and references therein). While a CIR ahead of an HSW is frequently detected near Earth, it evolves and becomes well-structured beyond ≈ 2.5 AU from the Sun (Gosling, Hundhausen, and Bame, 1976; Smith and Wolfe, 1976; Hajra et al., 2018; Hajra, 2021a, and references therein). HSW and CIR are known to cause geomagnetic disturbances at all latitudes (Verbanac et al., 2011b, 2013), especially high-intensity long-duration continuous auroral electrojet (AE) activities (HILDCAAs; Tsurutani and Gonzalez, 1987; Hajra et al., 2013). They also lead to magnetospheric relativistic electron acceleration (Hajra et al., 2015; Hajra and Tsurutani, 2018) and changes in thermospheric neutral density (Verbanac, Bandić, and Krauss, 2022, and references therein).

SSW at 1 AU is typically embedded in the heliospheric current sheet (HCS; Ness and Wilcox, 1964; Smith, Tsurutani, and Rosenberg, 1978), which is characterized by a simultaneous polarity reversal of the interplanetary magnetic field (IMF) B_x and B_y components in geocentric solar ecliptic (GSE) coordinate system and also approximately in geocentric solar magnetospheric (GSM) coordinate. The high plasma density region adjacent to the HCS is called the heliospheric plasma sheet (HPS; Winterhalter et al., 1994). HPS can compress the magnetosphere, causing a sudden and drastic loss of magnetospheric relativistic electrons to the atmosphere. For detailed mechanism of electron losses by HPS, the reader is referred to Tsurutani et al. (2016) and Hajra and Tsurutani (2018).

While general properties of HSW and SSW near Earth and their impacts on the Earth's magnetosphere-ionosphere-thermosphere are well explored, there is no comparative study on their statistical properties and geoeffectiveness. The latter is the aim of the present work. Based on all available near-Earth solar wind and geomagnetic measurements between 1963 and 2022, we will identify the typical solar wind and interplanetary features and geomagnetic impacts of HSW and SSW. We will also study the solar cycle dependencies, if any, of the solar wind parameters. The ≈ 59 -year period of this study covers more than five "Schwabe" solar activity cycles (Schwabe, 1844) with an average duration of ≈ 11 years. The robust statistical results will hopefully be useful for modeling solar winds and their geomagnetic impacts.

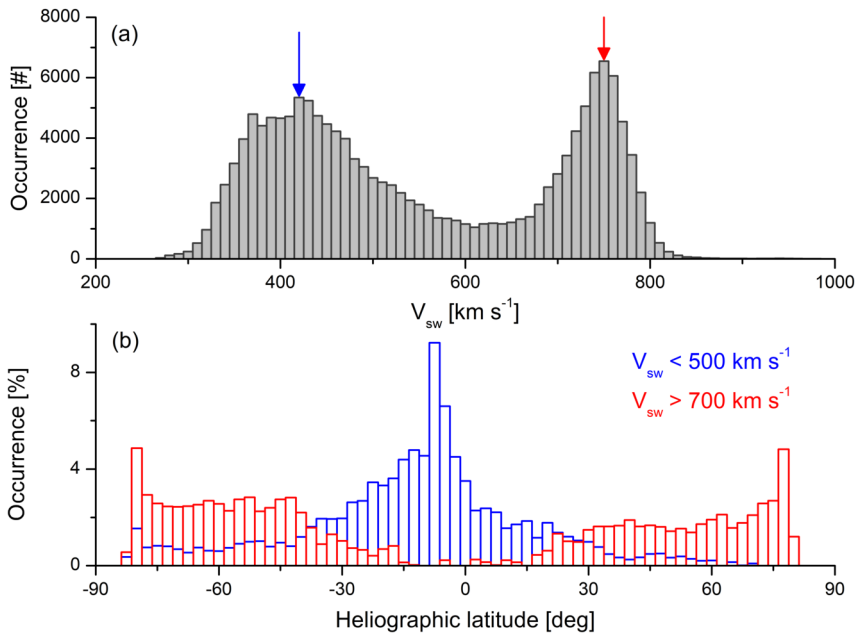


Figure 1 Solar wind observation by Ulysses. Distributions of (a) solar wind speed [V_{sw}], and (b) heliographic latitudes of Ulysses observing solar winds with $V_{sw} < 500 \text{ km s}^{-1}$ (blue) and $V_{sw} > 700 \text{ km s}^{-1}$ (red). Downward arrows indicate peaks of the V_{sw} distribution at $V_{sw} = 420 \text{ km s}^{-1}$ (blue) and 750 km s^{-1} (red).

2. Data Analyses and Results

2.1. SSW and HSW

The Ulysses spacecraft measured solar winds originating from equatorial to polar regions of the Sun between the heliocentric distance of ≈ 1.0 and ≈ 5.4 AU (McComas et al., 2000). Figure 1(a) shows distribution of plasma V_{sw} of all solar winds measured by Ulysses from 25 October 1990 to 30 June 2009. The data (1 hour resolution) are obtained from COHWeb (omniweb.gsfc.nasa.gov/coho/). Observed V_{sw} range from a minimum value of $\approx 269 \text{ km s}^{-1}$ to a maximum of 992 km s^{-1} is divided into bins of equal width of 10 km s^{-1} . The number of observations in each bin is shown in form of a histogram. Two prominent peaks of the distribution are observed at 420 km s^{-1} and 750 km s^{-1} (marked by blue and red downward arrows, respectively), indicating two different populations of solar wind. Based on this observation, solar winds can be separated into two groups: SSW with $V_{sw} < 500 \text{ km s}^{-1}$, and HSW with $V_{sw} > 700 \text{ km s}^{-1}$. Heliographic latitudes of Ulysses during observations of SSW and HSW are shown in Figure 1(b). While both SSW and HSW are found to have a large latitudinal extent, the SSW latitude peaks at -7.5° , and the HSW latitude peaks at -80.0° and $+77.5^\circ$. This result is consistent with equatorial and polar sources of SSW and HSW, respectively.

We will use the above-mentioned criteria of SSW and HSW (based on the Ulysses observations) to identify them near Earth (1 AU) and compare their near-Earth characteristic features and impacts on the Earth. The near-Earth solar wind and IMF measurements (1 hour resolution) from 27 November 1963 to 22 August 2022 are obtained from NASA's

OMNIWeb (omniweb.gsfc.nasa.gov/). These are solar winds measured by multiple spacecraft upstream of the Earth and propagated to Earth's bow shock nose. These are suitable to compare solar wind variations with associated geomagnetic impacts. IMFs in the GSM coordinates are considered, in which the origin is defined at the center of the Earth, the x -axis is directed towards the center of the Sun and the y -axis is in the $\mathbf{\Omega} \times \hat{\mathbf{x}}/|\mathbf{\Omega} \times \hat{\mathbf{x}}|$ direction, where $\mathbf{\Omega}$ is the geomagnetic dipole vector, and $\hat{\mathbf{x}}$ is the unit vector along the x -axis. The z -axis completes a right-hand system. The solar wind plasma characteristic parameters studied in this work are: plasma V_{sw} , proton number density $[N_p]$, alpha-to-proton density ratio $[N_a/N_p]$, ram pressure $[P_{sw}]$, proton temperature $[T_p]$, electric field $[E_{sw}]$, IMF magnitude $[B_0]$, and IMF north–south component $[B_z]$. The IMF southward component $[B_s]$ is computed as: $B_s = -B_z$ for $B_z < 0$ nT, and $B_s = 0$ for $B_z \geq 0$ nT. The reconnection electric field $[VB_s]$ is defined as: $VB_s = E_{sw}$ for $B_z < 0$ nT, and $VB_s = 0$ for $B_z \geq 0$ nT. Both B_s and VB_s are important parameters defining the geoeffectiveness of the solar wind (Burton, McPherron, and Russell, 1975; Tsurutani et al., 1992; Vršnak et al., 2017; Hajra, 2021b, and references therein). We also computed plasma- β [ratio of the plasma pressure to the magnetic pressure], sound speed $[V_s]$ ($\sqrt{5k_B(T_p + T_e)/3m_p}$), Alfvén speed $[V_A]$ ($B_0/\sqrt{\mu_0\rho}$), and magnetosonic speed $[V_{ms}]$ ($\sqrt{V_A^2 + V_s^2}$), where k_B is the Boltzmann constant, T_e is the electron temperature, m_p is the proton mass, μ_0 is the free space permeability, and ρ denotes the solar wind mass density. The Alfvén Mach number $[M_A]$ is defined as V_{sw}/V_A , and the magnetosonic Mach number $[M_{ms}]$ as V_{sw}/V_{ms} .

To study the geomagnetic conditions, we will use geomagnetic indices. The auroral electrojet index [AE] is important to study auroral ionospheric substorm activity. The geomagnetic Dst index shows the global-scale geomagnetic conditions associated with variations of ring currents. The geomagnetic indices (1 hour resolution) are obtained from the World Data Center for Geomagnetism, Kyoto, Japan (wdc.kugi.kyoto-u.ac.jp/).

2.2. Distributions

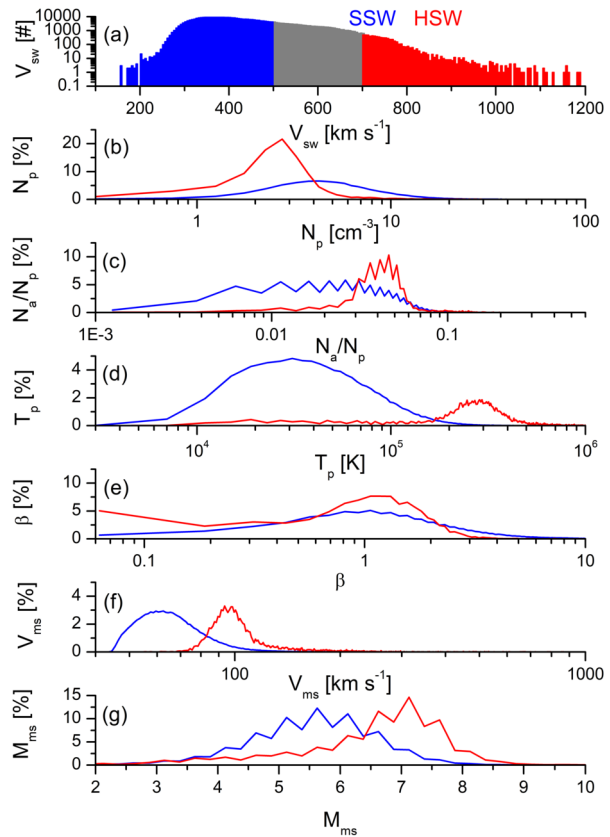
Distributions of different near-Earth solar wind/interplanetary parameters and geomagnetic indices for SSW and HSW are shown in Figures 2 and 3. The distributions are computed as follows. For each of the parameters, the range between the minimum and the maximum values is divided into bins of equal widths. Number of observations is counted for each of the bins. For V_{sw} , the distribution corresponds to the number of observations in each of the V_{sw} bins. For other parameters, percentages of observations are computed from the corresponding total observation counts (for the entire range). Statistical features of the distributions are summarized in Table 1.

Figure 2(a) shows the solar wind V_{sw} distribution for the entire period of study (1963–2022). V_{sw} varies from a minimum value of $\approx 156 \text{ km s}^{-1}$ to a maximum of $\approx 1189 \text{ km s}^{-1}$, with an average (median) speed of $\approx 433 \pm 102 \text{ km s}^{-1}$ ($\approx 410 \text{ km s}^{-1}$) for all solar winds. SSW constitutes $\approx 77\%$ of the entire solar wind distribution (blue), while HSW is only $\approx 2\%$ of the distribution (red).

SSW parameter distributions can be clearly distinguished from the HSW distributions. The differences in the SSW and HSW distributions are confirmed by estimated statistical probability factors or the p -values < 0.01 (not shown). The p -values are estimated based on the mean values and standard deviations of the parameters for SSW and HSW (Reiff, 1990; Press et al., 1992).

The HSW V_{sw} varies from 701 km s^{-1} to 1189 km s^{-1} (selection criteria), with an average V_{sw} of $\approx 750 \pm 52 \text{ km s}^{-1}$ for all HSW. On the other hand, for SSW, V_{sw} varies between

Figure 2 Near-Earth solar wind parameters. Distributions of (a) solar wind speed [V_{sw}], (b) proton density [N_p], (c) alpha-to-proton density ratio [N_a/N_p], (d) proton temperature [T_p], (e) plasma- β , (f) magnetosonic speed [V_{ms}], and (g) magnetosonic Mach number [M_{ms}]. Blue and red colors correspond to SSW and HSW, respectively.



156 km s⁻¹ and 499 km s⁻¹ (selection criteria), with an average V_{sw} of $\approx 388 \pm 55$ km s⁻¹. Thus, an $\approx 93\%$ increase is noted in average speed from SSW to HSW (Table 1).

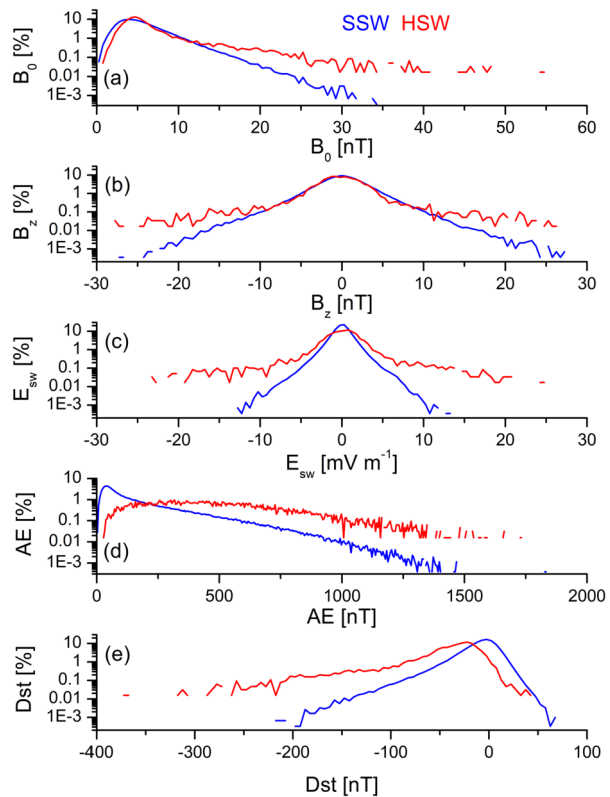
The HSW N_p distribution (Figure 2(b)) has a prominent peak around 2.8 cm⁻³, while it has much broader (flat) distribution for SSW with a peak at a higher value (4.3 cm⁻³). On average, HSW is characterized by $\approx 52\%$ lower N_p than SSW. On the other hand, HSW has $\approx 67\%$ higher average N_a/N_p than SSW (Figure 2(c)).

The most distinguishing feature between HSW and SSW is T_p (Figure 2(d)). The SSW T_p varies from 0.3×10^4 K to 289.9×10^4 K, with an average T_p of $\approx 7.1 \times 10^4$ K. The HSW T_p distribution is clearly distinguished with a minimum value of 0.6×10^4 K and a maximum value of 663.2×10^4 K, with an average T_p of $\approx 33.4 \times 10^4$ K. Thus, HSW is characterized by $\approx 370\%$ higher average T_p than SSW.

The computed V_s , V_A and V_{ms} are $> 50\%$ higher for HSW than for SSW, on average. HSW and SSW have distinguishing M_{ms} distributions (Figure 2(g)) with a peak at higher value for HSW (7.1) than for SSW (5.6). However, there are no significant differences in average Mach numbers (M_A and M_{ms}) identified between HSW and SSW (Table 1).

The distributions of the magnetic and electric fields are identical in shape for SSW and HSW, except that they have more extended tails (intense fields) for HSW (Figures 3(a)–(c)). Thus, differences in mean/median values between the distributions for SSW and HSW are small ($\leq 25\%$). While average B_s does not differ significantly between HSW and SSW, average $V B_s$ is significantly ($\approx 141\%$) stronger for HSW than for SSW.

Figure 3 Near-Earth solar wind and geomagnetic parameters. Distributions of (a) IMF magnitude [B_0], (b) IMF B_z component, (c) electric field [E_{sw}], (d) auroral electrojet index [AE], and (e) geomagnetic Dst index. Blue and red colors correspond to SSW and HSW, respectively.



The shapes of the AE and Dst distributions are identical between HSW and SSW (Figures 3(d)–(e)). However, the AE distribution has a stronger and longer tail at high AE values, and Dst has a stronger and longer tail at low Dst values for HSW. As a consequence, HSW has an average AE $\approx 213\%$ stronger and an average Dst $\approx 367\%$ stronger than those for SSW. Thus, HSW is characterized by stronger geomagnetic activity than SSW. This result is consistent with stronger $V B_s$ for HSW than for SSW.

2.3. Solar Cycle Variations

Figure 4 shows variations of the yearly occurrences of SSW and HSW, and their yearly mean speeds. Variation of the $F_{10.7}$ solar radio flux, a proxy for solar activity, indicates more than five solar cycles (SC), from the SC 20 minimum to the SC 25 ascending phase (Figure 4(c)). The yearly mean $F_{10.7}$ solar flux data are obtained from the Laboratory for Atmospheric and Space Physics (LASP) Interactive Solar Irradiance Data Center (lasp.colorado.edu/lisird/). The yearly average V_{sw} for all solar winds (Figure 4(c)) shows prominent peaks around the descending to minimum phases of the cycles. SSW is observed in every phase of the solar cycle, without any prominent solar cycle phase dependence (Figure 4(b)). The lowest and the highest SSW occurrences are recorded during SC 22 and SC 24, which are the strongest and the weakest solar cycles of the space age, respectively (see Hajra, 2021c). Three prominent peaks are observed in the HSW occurrence (Figure 4(a)), during the minimum between SC 20 and SC 21, the minimum between SC 22 and SC 23, and during the descending phase

Table 1 Statistical properties and geoeffectiveness of SSW and HSW.

Parameter	SSW		HSW		Increase ^a
	Mean $\pm \sigma$	Median	Mean $\pm \sigma$	Median	
V_{sw} [km s ⁻¹]	388 \pm 55	385	750 \pm 52	737	93% (91%)
N_p [cm ⁻³]	7.5 \pm 5.7	5.9	3.6 \pm 3.7	2.8	-52% (-53%)
N_a/N_p	0.03 \pm 0.02	0.03	0.05 \pm 0.02	0.04	67% (33%)
P_{sw} [nPa]	2.1 \pm 1.6	1.7	4.1 \pm 5.1	3.0	95% (76%)
T_p [$\times 10^4$ K]	7.1 \pm 5.6	5.7	33.4 \pm 26.3	29.4	370% (416%)
β	2.8 \pm 5.0	1.7	1.3 \pm 0.8	1.2	-54% (-29%)
B_0 [nT]	5.3 \pm 2.8	4.7	6.6 \pm 5.3	5.1	25% (9%)
B_s [nT]	2.2 \pm 2.1	1.6	2.7 \pm 3.5	1.7	23% (6%)
$V B_s$ [mV m ⁻¹]	0.85 \pm 0.87	0.60	2.05 \pm 2.90	1.26	141% (110%)
V_A [km s ⁻¹]	45 \pm 27	40	79 \pm 67	61	76% (53%)
V_S [km s ⁻¹]	53 \pm 7	52	80 \pm 17	78	51% (50%)
V_{ms} [km s ⁻¹]	71 \pm 22	67	117 \pm 60	100	65% (49%)
M_A	9.9 \pm 5.3	8.8	9.5 \pm 3.0	9.8	-4% (11%)
M_{ms}	5.5 \pm 1.0	5.6	6.4 \pm 1.4	6.8	16% (21%)
AE [nT]	158 \pm 172	89	494 \pm 292	448	213% (403%)
Dst [nT]	-9 \pm 17	-7	-42 \pm 39	-32	367% (357%)

^aIncrease from the SSW mean (median) values to the HSW mean (median) values.

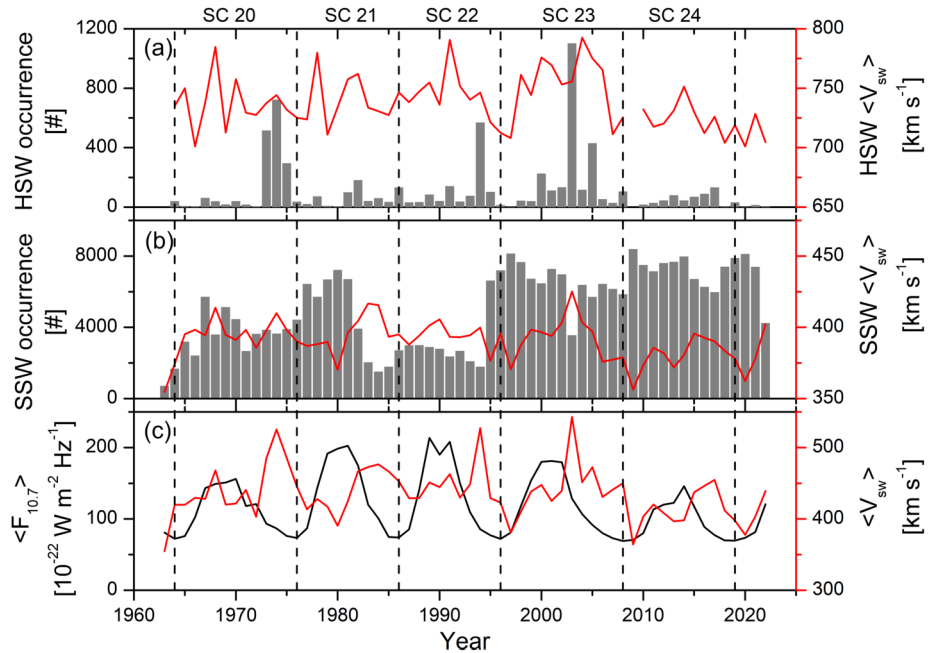
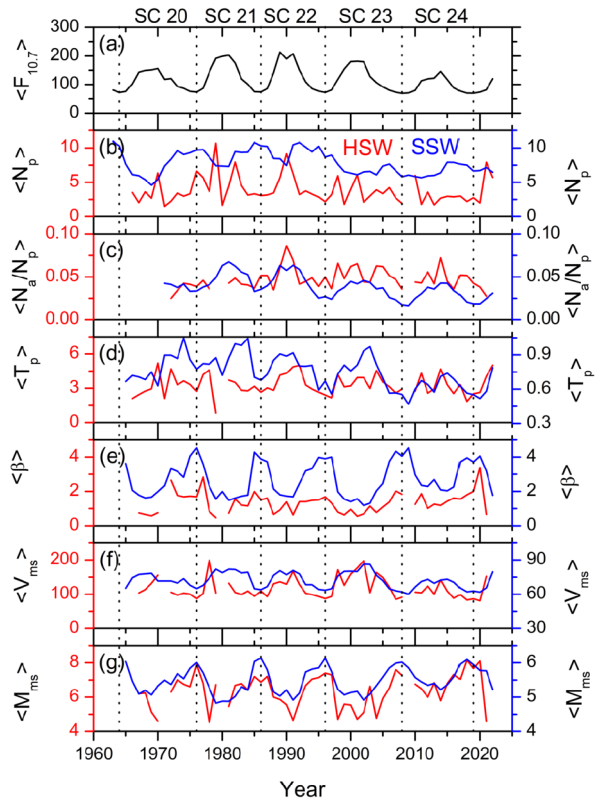


Figure 4 Solar-cycle variation of solar winds. Yearly variations of (a) HSW occurrence (histogram, scale on the left), and HSW V_{sw} (red, scale on the right), (b) SSW occurrence (histogram, scale on the left), and SSW V_{sw} (red, scale on the right), (c) $F_{10.7}$ solar flux (black, scale on the left) and average V_{sw} for all solar winds (red, scale on the right). Vertical dashed lines indicate the solar cycle minima, and the solar cycle (SC) numbers are marked at the top.

Figure 5 Solar-cycle variation of solar wind parameters. Yearly variations of (a) $F_{10.7}$ solar flux, (b) solar wind N_p , (c) N_a/N_p , (d) T_p , (e) plasma- β , (f) V_{ms} , and (g) M_{ms} . Blue and red colors correspond to SSW and HSW, respectively.



of SC 23. There are no significant correlations of the SSW V_{sw} and HSW V_{sw} with the $F_{10.7}$ solar flux variations (Table 2).

The solar cycle variations of the solar wind and geomagnetic parameters are shown in Figures 5 and 6. Table 2 lists the correlation coefficients (r) of the parameters with the $F_{10.7}$ solar fluxes, and corresponding confidence levels (c) for SSW and HSW.

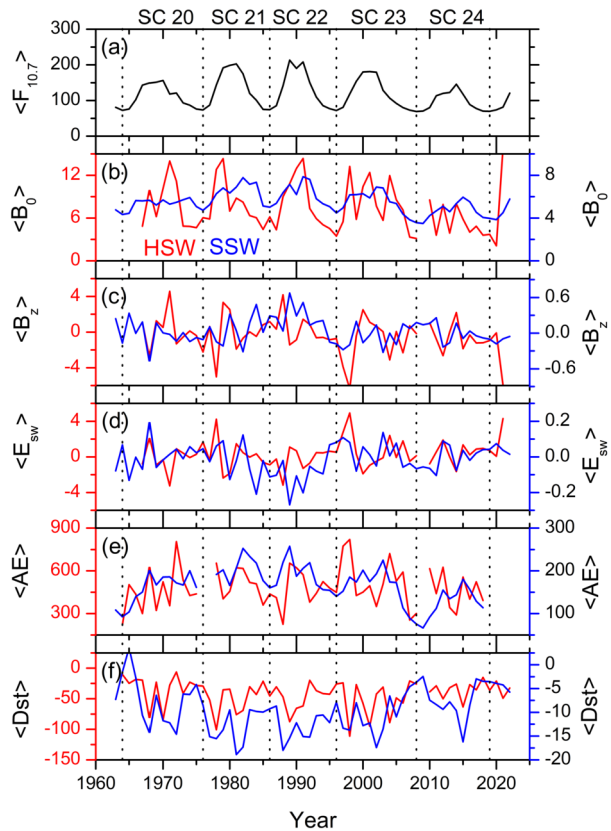
All the parameters are slightly stronger for HSW than for SSW, except N_p and β which are stronger for SSW. This result is consistent with results presented in Figures 2, 3 and Table 1. The SSW N_p values are significantly higher than the HSW N_p values throughout the solar cycles, except around the solar maxima (Figure 5(b)). With increasing $F_{10.7}$, N_p exhibits a decreasing trend for SSW and an increasing trend for HSW. However, the correlation/anti-correlation coefficients are poor (Table 2), indicating no significant solar cycle dependence of N_p .

For SSW, the solar wind parameters N_a/N_p (Figure 5(c)), T_p (Figure 5(d)), B_0 (Figure 6(b)), V_A (not shown), V_S (not shown), and V_{ms} (Figure 5(f)) exhibit medium to strong correlations (correlation coefficients $r = 0.51$ to 0.87) with $F_{10.7}$, and β (Figure 5(e)), M_A (not shown), and M_{ms} (Figure 5(g)) exhibit strong anti-correlations ($r = -0.82$ to -0.90) with $F_{10.7}$ (Table 2). The associations are significantly weaker for HSW.

3. Summary and Discussions

All near-Earth solar wind plasma and IMF measurements from 1963 through 2022 are analyzed to compare the characteristic features of HSW and SSW with average speeds of

Figure 6 Solar-cycle variation of solar wind and geomagnetic parameters. Yearly variations of (a) $F_{10.7}$ solar flux, (b) IMF B_0 , (c) IMF B_z component, (d) E_{sw} , (e) AE, and (f) Dst. Blue and red colors correspond to SSW and HSW, respectively.



$\approx 750 \pm 52 \text{ km s}^{-1}$ and $\approx 388 \pm 55 \text{ km s}^{-1}$, respectively. The geomagnetic indices are explored to compare their geomagnetic impacts. In addition, the ≈ 5.5 -solar cycle-long measurements are utilized to identify the solar cycle variations of the solar wind characteristics and their geomagnetic impacts. The main results are summarized below.

- i) On average, HSW is characterized by $\approx 67\%$ higher N_a/N_p , $\approx 95\%$ higher P_{sw} , $\approx 370\%$ higher T_p , $\approx 141\%$ higher $V B_s$, $\approx 76\%$ higher V_A , $\approx 65\%$ higher V_{ms} , and $\approx 52\%$ lower N_p and $\approx 54\%$ lower plasma- β than SSW.
- ii) The geomagnetic activity is found to be enhanced during HSW, as reflected in $\approx 213\%$ higher AE and $\approx 367\%$ stronger Dst during HSW than those during SSW.
- iii) The SSW characteristic parameters N_a/N_p , T_p , B_0 , V_A , and V_{ms} exhibit medium to strong correlations (correlation coefficients $r = 0.51$ to 0.87) with the $F_{10.7}$ solar radio flux, while plasma- β and the Mach numbers exhibit strong anti-correlations ($r = -0.82$ to -0.90) with $F_{10.7}$. The associations are weaker or insignificant for HSW.

HSW is found to be only a small ($\approx 2\%$) fraction of all solar winds, SSW is $\approx 77\%$ of the entire solar wind distribution, and $\approx 21\%$ have intermediate speeds between 500 km s^{-1} and 700 km s^{-1} . The yearly average solar wind speed for all solar winds are found to peak during the descending phase of the solar cycle. However, HSW V_{sw} and SSWs V_{sw} do not exhibit any clear solar cycle dependence. This result indicates plausible complex solar sources of HSW and SSW.

Table 2 Association of the yearly mean solar wind and geomagnetic parameters with the yearly mean $F_{10.7}$ solar flux.

Parameter	SSW		HSW	
	Correlation Coefficient [r]	Confidence Level [c]	Correlation Coefficient [r]	Confidence Level [c]
V_{sw}	0.34	> 99.0%	0.45	> 99.9%
N_p	-0.21	> 80.0%	0.22	> 80.0%
N_a/N_p	0.83	> 99.9%	0.45	> 99.8%
P_{sw}	0.08	< 50.0%	0.30	> 95.0%
T_p	0.51	> 99.9%	0.35	> 99.0%
β	-0.82	> 99.9%	-0.61	> 99.9%
B_0	0.76	> 99.9%	0.57	> 99.9%
B_z	0.19	> 80.0%	0.25	> 90.0%
E_{sw}	-0.19	> 80.0%	-0.24	> 90.0%
V_A	0.87	> 99.9%	0.65	> 99.9%
V_S	0.51	> 99.9%	0.26	> 90.0%
V_{ms}	0.84	> 99.9%	0.60	> 99.9%
M_A	-0.87	> 99.9%	-0.71	> 99.9%
M_{ms}	-0.90	> 99.9%	-0.66	> 99.9%
AE	0.65	> 99.9%	0.15	> 70.0%
Dst	-0.65	> 99.9%	-0.46	> 99.9%

The near-Earth HSW identified with the criteria $V_{sw} > 700 \text{ km s}^{-1}$ can have two possible sources. It can be “hot, high-velocity” plasma stream (Neugebauer and Snyder, 1966; Belcher and Davis, 1971) emanated from a solar equatorial coronal hole (Krieger, Timothy, and Roelof, 1973). It may have speeds of $\approx 750\text{--}800 \text{ km s}^{-1}$ near the Sun (e.g. Phillips et al., 1995). Another source of the HSW can be fast ($V_{sw} > 500 \text{ km s}^{-1}$) interplanetary coronal mass ejections (ICMEs) associated with solar flares (Sheeley, Harvey, and Feldman, 1976; Tang et al., 1989). ICMEs can have impulsive speeds up to a few 1000 km s^{-1} (Carrington, 1859; Cliver, Feynman, and Garrett, 1990; Tsurutani et al., 2003). While equatorial coronal holes are a dominant solar feature of the solar cycle descending phase and solar minimum, solar flares or ICMEs occur predominantly during solar maximum and a few years after the maximum. As a result, we identified three major peaks in the HSW occurrence (Figure 4(a)), namely, around the minimum between SC 20 and SC 21, the minimum between SC 22 and SC 23, and following the maximum of SC 23. Extremely low number of HSW is recorded during SC 24, which is the weakest of all solar cycles of the space age (Hajra, 2021c) with very low numbers of ICMEs (Scolini et al., 2018; Lamy et al., 2019; Syed Ibrahim et al., 2019) and coronal hole emanated streams (Grandin, Aikio, and Kozlovsky, 2019; Nakagawa, Nozawa, and Shinbori, 2019). The high geomagnetic activity during HSW observed in this work may be due to the high geoeffectiveness of the fast ICMEs and coronal hole emanated streams with preceding CIRs. While HSW is contributed to by coronal hole emanated streams and fast ICMEs, the plasma and IMF characteristics are significantly different between the two. In addition, they have significantly different solar cycle dependencies. As a result, HSW characteristic features exhibit poor association with the $F_{10.7}$ solar flux variation.

On the other hand, the near-Earth SSW (with $V_{sw} < 500 \text{ km s}^{-1}$) may originate from a solar helmet streamer. It also may be the trailing portion of a coronal hole emanated HSW,

where a rarefaction region with decreased N_p , T_p , and IMF B_0 is created (Sarabhai, 1963; Parker, 1965; Tsurutani, Echer, and Gonzalez, 2011; Hajra and Tsurutani, 2022). However, it should be noted that the SSW is found to be characterized by high N_p , not expected in an HSW rarefaction region. Recently, Tsurutani and Hajra (2022) studied all extremely slow solar winds (ESSWs) with $V_{sw} < 300 \text{ km s}^{-1}$ from 1963 through 2021. The ESSWs are reported to be terminated by high- N_p plasmas associated with CIRs or HPSs. Another contributor of the SSW can be slow ($\approx 350\text{--}400 \text{ km s}^{-1}$) ICMEs (Tsurutani et al., 2004) associated with magnetic reconnection at the edges of coronal holes (Chen, 2011). Weak geomagnetic activity associated with SSW can be due to lack of space weather events (such as CIRs or ICMEs) that can provide B_s during SSW. This can also explain clear association of the SSW characteristic features with the solar cycle $F_{10.7}$ variation.

Acknowledgments The work is funded by the Science and Engineering Research Board (SERB, grant no. SB/S2/RJN-080/2018), a statutory body of the Department of Science and Technology (DST), Government of India through the Ramanujan Fellowship.

Author contributions I am the sole author of this paper.

Data Availability The Ulysses solar wind data are obtained from COHWeb (omniweb.gsfc.nasa.gov/coho/). The near-Earth solar wind and IMF measurements are obtained from OMNIWeb (omniweb.gsfc.nasa.gov/). The geomagnetic indices are obtained from the World Data Center for Geomagnetism, Kyoto, Japan (wdc.kugi.kyoto-u.ac.jp/). The $F_{10.7}$ solar flux data are obtained from the Laboratory for Atmospheric and Space Physics (LASP) Interactive Solar Irradiance Data Center (lasp.colorado.edu/lisird/).

Declarations

Competing interests The authors declare no competing interests.

References

- Abbo, L., Ofman, L., Antiochos, S.K., Hansteen, V.H., Harra, L., Ko, Y.-K., Lapenta, G., Li, B., Riley, P., Strachan, L., von Steiger, R., Wang, Y.-M.: 2016, Slow solar wind: observations and modeling. *Space Sci. Rev.* **201**, 55. DOI.
- Belcher, J.W., Davis, L. Jr.: 1971, Large-amplitude Alfvén waves in the interplanetary medium, 2. *J. Geophys. Res.* **76**, 3534. DOI.
- Burlaga, L.F.: 1974, Interplanetary stream interfaces. *J. Geophys. Res.* **79**, 3717. DOI.
- Burlaga, L.F., Behannon, K.W., Hansen, S.F., Pneuman, G.W., Feldman, W.C.: 1978, Sources of magnetic fields in recurrent interplanetary streams. *J. Geophys. Res.* **83**, 4177. DOI.
- Burton, R.K., McPherron, R.L., Russell, C.T.: 1975, An empirical relationship between interplanetary conditions and Dst. *J. Geophys. Res.* **80**, 4204. DOI.
- Carrington, R.C.: 1859, Description of a Singular Appearance seen in the Sun on September 1, 1859. *Mon. Not. Roy. Astron. Soc.* **20**, 13. DOI.
- Chen, P.F.: 2011, Coronal mass ejections: models and their observational basis. *Living Rev. Solar Phys.* **8**, 1. DOI.
- Cliver, E.W., Feynman, J., Garrett, H.B.: 1990, An estimate of the maximum speed of the solar wind, 1938–1989. *J. Geophys. Res.* **95**, 17103. DOI.
- D’Amicis, R., Perrone, D., Bruno, R., Velli, M.: 2021, On Alfvénic slow wind: a journey from the Earth back to the Sun. *J. Geophys. Res.* **126**, e2020JA028996. DOI.
- Davis, L. Jr.: 1966, Models of interplanetary fields and plasma flow. In: Mackin, R.J., Neugebauer, M. (eds.) *The Solar Wind*, Pergamon Press, New York, 147.
- Davis, L. Jr., Smith, E.J., Coleman, P.J., Sonett, C.P.: 1966, Interplanetary magnetic measurements. In: Mackin, R.J., Neugebauer, M. (eds.) *The Solar Wind*, Pergamon Press, New York, 35.
- Gosling, J.T., Hundhausen, A.J., Bame, S.J.: 1976, Solar wind stream evolution at large heliocentric distances: experimental demonstration and the test of a model. *J. Geophys. Res.* **81**, 2111. DOI.

- Gosling, J.T., Asbridge, J.R., Bame, S.J., Feldman, W.C.: 1978, Solar wind stream interfaces. *J. Geophys. Res.* **83**, 1401. [DOI](#).
- Gosling, J.T., Borrini, G., Asbridge, J.R., Bame, S.J., Feldman, W.C., Hansen, R.T.: 1981, Coronal streamers in the solar wind at 1 AU. *J. Geophys. Res.* **86**, 5438. [DOI](#).
- Grandin, M., Aikio, A.T., Kozlovsky, A.: 2019, Properties and geoeffectiveness of solar wind high-speed streams and stream interaction regions during solar cycles 23 and 24. *J. Geophys. Res.* **124**, 3871. [DOI](#).
- Hajra, R.: 2021a, Variation of the interplanetary shocks in the inner heliosphere. *Astrophys. J.* **917**, 91. [DOI](#).
- Hajra, R.: 2021b, September 2017 space-weather events: a study on magnetic reconnection and geoeffectiveness. *Solar Phys.* **296**, 50. [DOI](#).
- Hajra, R.: 2021c, Weakest solar cycle of the space age: a study on solar wind–magnetosphere energy coupling and geomagnetic activity. *Solar Phys.* **296**, 33. [DOI](#).
- Hajra, R., Sunny, J.V.: 2022, Corotating interaction regions during solar cycle 24: a study on characteristics and geoeffectiveness. *Solar Phys.* **297**, 30. [DOI](#).
- Hajra, R., Tsurutani, B.T.: 2018, Interplanetary shocks inducing magnetospheric supersubstorms ($SML < -2500$ nT): unusual auroral morphologies and energy flow. *Astrophys. J.* **858**, 123. [DOI](#).
- Hajra, R., Tsurutani, B.T.: 2022, Near-Earth sub-Alfvénic solar winds: interplanetary origins and geomagnetic impacts. *Astrophys. J.* **926**, 135. [DOI](#).
- Hajra, R., Echer, E., Tsurutani, B.T., Gonzalez, W.D.: 2013, Solar cycle dependence of high-intensity long-duration continuous AE activity (HILDCAA) events, relativistic electron predictors? *J. Geophys. Res.* **118**, 5626. [DOI](#).
- Hajra, R., Tsurutani, B.T., Echer, E., Gonzalez, W.D., Santolik, O.: 2015, Relativistic ($E > 0.6$, > 2.0 , and > 4.0 MeV) electron acceleration at geosynchronous orbit during high-intensity, long-duration, continuous AE activity (HILDCAA) events. *Astrophys. J.* **799**, 39. [DOI](#).
- Hajra, R., Henri, P., Myllys, M., Héritier, K.L., Galand, M., Simon Wedlund, C., Breuillard, H., Behar, E., Edberg, N.J.T., Goetz, C., Nilsson, H., Eriksson, A.I., Goldstein, R., Tsurutani, B.T., Moré, J., Vallières, X., Wattieaux, G.: 2018, Cometary plasma response to interplanetary corotating interaction regions during 2016 June–September: a quantitative study by the Rosetta Plasma Consortium. *Mon. Not. Roy. Astron. Soc.* **480**, 4544. [DOI](#).
- Krieger, A.S., Timothy, A.F., Roelof, E.C.: 1973, A coronal hole and its identification as the source of a high velocity solar wind stream. *Solar Phys.* **29**, 505. [DOI](#).
- Lamy, P.L., Floyd, O., Boclet, B., Wojak, J., Gilardy, H., Barlyaeva, T.: 2019, Coronal mass ejections over solar cycles 23 and 24. *Space Sci. Rev.* **215**, 39. [DOI](#).
- McComas, D.J., Barraclough, B.L., Funsten, H.O., Gosling, J.T., Santiago-Muñoz, E., Skoug, R.M., Goldstein, B.E., Neugebauer, M., Riley, P., Balogh, A.: 2000, Solar wind observations over Ulysses' first full polar orbit. *J. Geophys. Res.* **105**, 10419. [DOI](#).
- Nakagawa, Y., Nozawa, S., Shinbori, A.: 2019, Relationship between the low-latitude coronal hole area, solar wind velocity, and geomagnetic activity during solar cycles 23 and 24. *Earth Planets Space* **71**, 24. [DOI](#).
- Ness, N.F., Wilcox, J.M.: 1964, Solar origin of the interplanetary magnetic field. *Phys. Rev. Lett.* **13**, 461. [DOI](#).
- Neugebauer, M., Snyder, C.W.: 1966, Mariner 2 observations of the solar wind: 1. Average properties. *J. Geophys. Res.* **71**, 4469. [DOI](#).
- Parker, E.N.: 1965, Dynamical theory of the solar wind. *Space Sci. Rev.* **4**, 666. [DOI](#).
- Phillips, J.L., Bame, S.J., Feldman, W.C., Gosling, J.T., Hammond, C.M., McComas, D.J., Goldstein, B.E., Neugebauer, M., Scime, E.E., Suess, S.T.: 1995, Ulysses solar wind plasma observations at high southerly latitudes. *Science* **268**, 1030. [DOI](#).
- Pizzo, V.J.: 1985, In: Tsurutani, B.T., Stone, R.G. (eds.) *Interplanetary Shocks on the Large Scale: A Retrospective on the Last Decade's Theoretical Efforts* 35, AGU, Washington, 51.
- Press, W.H., Teukolsky, S.A., Vetterling, W.T., Flannery, B.P.: 1992, *Numerical Recipes in C: The Art of Scientific Computing*, 2nd edn. Cambridge University Press, Cambridge, 0521431085.
- Reiff, P.H.: 1990, The use and misuse of statistics in space physics. *J. Geomagn. Geoelectr.* **42**, 1145. [DOI](#).
- Richardson, I.G., Cliver, E.W., Cane, H.V.: 2000, Sources of geomagnetic activity over the solar cycle: relative importance of coronal mass ejections, high-speed streams, and slow solar wind. *J. Geophys. Res.* **105**, 18203. [DOI](#).
- Sanchez-Diaz, E., Rouillard, A.P., Lavraud, B., Segura, K., Tao, C., Pinto, R., Sheeley, N.R. Jr, Plotnikov, I.: 2016, The very slow solar wind: properties, origin and variability. *J. Geophys. Res.* **121**, 2830. [DOI](#).
- Sarabhai, V.: 1963, Some consequences of nonuniformity of solar wind velocity. *J. Geophys. Res.* **68**, 1555. [DOI](#).
- Schwabe, H.: 1844, Sonnen — Beobachtungen im Jahre 1843. *Astron. Nachr.* **21**, 234. [DOI](#).
- Scolini, C., Messerotti, M., Poedts, S., Rodriguez, L.: 2018, Halo coronal mass ejections during Solar Cycle 24: reconstruction of the global scenario and geoeffectiveness. *J. Space Weather Space Clim.* **8**, A09. [DOI](#).

- Sheeley, N.R., Harvey, J.W.: 1981, Coronal holes, solar wind streams, and geomagnetic disturbances during 1978 and 1979. *Solar Phys.* **70**, 237. [DOI](#).
- Sheeley, N.R., Harvey, J.W., Feldman, W.C.: 1976, Coronal holes, solar wind streams, and recurrent geomagnetic disturbances: 1973–1976. *Solar Phys.* **49**, 271. [DOI](#).
- Smith, E.J., Tsurutani, B.T., Rosenberg, R.L.: 1978, Observations of the interplanetary sector structure up to heliographic latitudes of 16° : pioneer 11. *J. Geophys. Res.* **83**, 717. [DOI](#).
- Smith, E.J., Wolfe, J.H.: 1976, Observations of interaction regions and corotating shocks between one and five AU: pioneers 10 and 11. *Geophys. Res. Lett.* **3**, 137. [DOI](#).
- Suess, S.T., Ko, Y.-K., von Steiger, R., Moore, R.L.: 2009, Quiescent current sheets in the solar wind and origins of slow wind. *J. Geophys. Res.* **114**, A04103. [DOI](#).
- Sunny, J.V., Nair, A.G., Babu, M., Hajra, R.: 2023, A comparative study on geoeffective and non-geoeffective corotating interaction regions. *Adv. Space Res.* **71**, 268. [DOI](#).
- Syed Ibrahim, M., Joshi, B., Cho, K.-S., Kim, R.-S., Moon, Y.-J.: 2019, Interplanetary coronal mass ejections during solar cycles 23 and 24: Sun–Earth propagation characteristics and consequences at the near–Earth region. *Solar Phys.* **294**, 54. [DOI](#).
- Tang, F., Tsurutani, B.T., Gonzalez, W.D., Akasofu, S.I., Smith, E.J.: 1989, Solar sources of interplanetary southward Bz events responsible for major magnetic storms (1978–1979). *J. Geophys. Res.* **94**, 3535. [DOI](#).
- Tsurutani, B.T., Echer, E., Gonzalez, W.D.: 2011, The solar and interplanetary causes of the recent minimum in geomagnetic activity (MGA23): a combination of midlatitude small coronal holes, low IMF Bz variances, low solar wind speeds and low solar magnetic fields. *Ann. Geophys.* **29**, 839. [DOI](#).
- Tsurutani, B.T., Gonzalez, W.D.: 1987, The cause of high-intensity long-duration continuous AE activity (HILDCAAs): interplanetary Alfvén wave trains. *Planet. Space Sci.* **35**, 405. [DOI](#).
- Tsurutani, B.T., Hajra, R.: 2022, Extremely slow ($V_{sw} < 300 \text{ km s}^{-1}$) solar winds (ESSWs) at 1 au: causes of extreme geomagnetic quiet at Earth. *Astrophys. J.* **936**, 155. [DOI](#).
- Tsurutani, B.T., Gonzalez, W.D., Tang, F., Lee, Y.T.: 1992, Great magnetic storms. *Geophys. Res. Lett.* **19**, 73. [DOI](#).
- Tsurutani, B.T., Gonzalez, W.D., Lakhina, G.S., Alex, S.: 2003, The extreme magnetic storm of 1–2 September 1859. *J. Geophys. Res.* **108**, 1268. [DOI](#).
- Tsurutani, B.T., Gonzalez, W.D., Zhou, X.-Y., Lepping, R.P., Bothmer, V.: 2004, Properties of slow magnetic clouds. *J. Atmos. Solar-Terr. Phys.* **66**, 147. [DOI](#).
- Tsurutani, B.T., Gonzalez, W.D., Gonzalez, A.L.C., Guarnieri, F.L., Gopalswamy, N., Grande, M., Kamide, Y., Kasahara, Y., Lu, G., Mann, I., McPherron, R., Soraas, F., Vasyliunas, V.: 2006, Corotating solar wind streams and recurrent geomagnetic activity: a review. *J. Geophys. Res.* **111**, A07S01. [DOI](#).
- Tsurutani, B.T., Hajra, R., Tanimori, T., Takada, A., Remya, B., Mannucci, A.J., Lakhina, G.S., Kozyra, J.U., Shiokawa, K., Lee, L.C., Echer, E., Reddy, R.V., Gonzalez, W.D.: 2016, Heliospheric plasma sheet (HPS) impingement onto the magnetosphere as a cause of relativistic electron dropouts (REDs) via coherent EMIC wave scattering with possible consequences for climate change mechanisms. *J. Geophys. Res.* **121**, 10130. [DOI](#).
- Verbanac, G., Bandić, M., Krauss, S.: 2022, Influence of the solar wind high-speed streams on the thermospheric neutral density during the declining phase of solar cycle 23. *Adv. Space Res.* **69**, 4335. [DOI](#).
- Verbanac, G., Vršnak, B., Veronig, A., Temmer, M.: 2011a, Equatorial coronal holes, solar wind high-speed streams, and their geoeffectiveness. *Astron. Astrophys.* **526**, A20. [DOI](#).
- Verbanac, G., Vršnak, B., Živković, S., Hojsak, T., Veronig, A.M., Temmer, M.: 2011b, Solar wind high-speed streams and related geomagnetic activity in the declining phase of solar cycle 23. *Astron. Astrophys.* **533**, A49. [DOI](#).
- Verbanac, G., Živković, S., Vršnak, B., Bandić, M., Hojsak, T.: 2013, Comparison of geoeffectiveness of coronal mass ejections and corotating interaction regions. *Astron. Astrophys.* **558**, A85. [DOI](#).
- Vršnak, B., Temmer, M., Veronig, A.M.: 2007, Coronal holes and solar wind high-speed streams: II. Forecasting the geomagnetic effects. *Solar Phys.* **240**, 331. [DOI](#).
- Vršnak, B., Dumbović, M., Čalogović, J., Verbanac, G., Poljanić–Beljan, I.: 2017, Geomagnetic effects of corotating interaction regions. *Solar Phys.* **292**, 140. [DOI](#).
- Winterhalter, D., Smith, E.J., Burton, M.E., Murphy, N., McComas, D.J.: 1994, The heliospheric plasma sheet. *J. Geophys. Res.* **99**, 6667. [DOI](#).